Estimation of velocity vectors in synthetic aperture ultrasound imaging

Jensen, Jørgen Arendt; Oddershede, Niels

Published in:
I E E E Transactions on Medical Imaging

Link to article, DOI:
10.1109/TMI.2006.883087

Publication date:
2006

Document Version
Publisher's PDF, also known as Version of record

Estimation of Velocity Vectors in Synthetic Aperture Ultrasound Imaging

Jørgen Arendt Jensen* and Niels Oddershede

***Abstract*—A method for determining both velocity magnitude and angle in a synthetic aperture ultrasound system is described. The approach uses directional beamforming along the flow direction and cross correlation to determine velocity magnitude. The angle of the flow is determined from the maximum normalized correlation calculated as a function of angle. This assumes the flow direction is within the imaging plane. Simulations of the angle estimation method show both biases and standard deviations of the flow angle estimates below 3° for flow angles from 20° to 90° (transverse flow). The method is also investigated using data measured by an experimental ultrasound scanner from a flow rig. A commercial 128 element 7-MHz linear array transducer is used, and data are measured for flow angles of 60° and 90°. Data are acquired using the RASMUS experimental ultrasound scanner, which samples 64 channels simultaneously. A 20-μs chirp was used during emission and eight virtual transmit sources were created behind the transducer using 11 transmitting elements. Data from the eight transmissions are beamformed and coherently summed to create high-resolution lines at different angles for a set of points within the region of flow. The velocity magnitude is determined with a precision of 0.36% (60°) and 1.2% (90°), respectively. The 60° angle is estimated with a bias of 0.54° and a standard deviation of 2.1°. For 90° the bias is 0.0003° and standard deviation 1.32°. A parameter study with regard to correlation length and number of emissions is performed to reveal the accuracy of the method. Real time data covering 2.2 s of the carotid artery of a healthy 30-year-old male volunteer is acquired and then processed offline using a computer cluster. The direction of flow is estimated using the above mentioned method. It is compared to the flow angle of 106° with respect to the axial direction, determined visually from the B-mode image. For a point in the center of the common carotid artery, 76% of the flow angle estimates over the 2.2 s were within 10° of the visually determined flow angle. The standard deviation of these estimates was below 2.7°. Full color flow maps from different parts of the cardiac cycle are presented, including vector arrows indicating both estimated flow direction and velocity magnitude.**

***Index Terms*—Angle determination, medical ultrasound, synthetic aperture, vector velocity estimation.**

I. Introduction

CURRENT ultrasound velocity estimation systems only estimate the blood velocity projected onto the direction of the steered ultrasound beam [1], [2]. The velocities are, thus, only found in one direction in the image, and velocities in the direction perpendicular to the beam cannot be estimated. Neither the correct velocity magnitude nor the velocity angle are, thus, estimated.

A two-dimensional (2-D) velocity estimation system should be able to give both velocity magnitude and direction [3]–[5]. A directional beamforming approach was suggested for conventional ultrasound imaging in [6] and for synthetic aperture (SA) flow imaging in [7] and [8]. Here, the received echoes are dynamically focused in points along a line following the direction of the flow. A cross-correlation estimator is then used to find the velocity magnitude along the flow direction. In these papers, the angle for the beam processing is, however, manually determined from the B-mode image before beamforming.

This paper presents a method for also estimating the velocity angle in a SA flow system as originally suggested in [9]. The procedure determines both velocity magnitude and angle using cross correlation of the received signals, and it can be employed for estimation of both blood velocity and tissue motion. This paper will described the method in details and give data for its performance for simulated data, measured data from a flow rig, and *in vivo* data. The basic principle of directional synthetic aperture flow imaging is described in Section II and the angle determination procedure is detailed in Section III. In Section IV, simulations of the angle determination method is presented for a wide range of flow angles. The performance of the approach is determined in Section V from data measured using an experimental ultrasound scanner and a flow rig, and a parameter study is given in Section VI. Finally, examples of vector velocity images are presented in Section VII for flow rig data and for *in vivo* data from the carotid artery in Section VIII.

II. Method for SA Flow Imaging

SA ultrasound images are acquired by emitting a spherical wave with one or a collection of transducer elements [10], [11]. The scattered signals are then received by all transducer elements, and a low-resolution image is generated by focusing the received signal in all points of the image. The process is repeated for other sets of transmitting elements and new low-resolution images are formed. Combining all low-resolution images will give a high-resolution image, that is dynamically focused in both transmit and receive, thus, yielding a higher resolution than traditional images, if a sufficient number of transmissions N_t are used [12]. A new high-resolution image can be formed after each transmission, if the transmission sequence is repeated. The oldest transmission event is then replaced by the newest, and the imaging can therefore be done recursively [13].

SA images can also be used for flow estimation, if the data collection is repeated. Data from two high-resolution images

Manuscript received June 15, 2006; revised July 20, 2006. This work was supported by the Danish Science Foundation under Grant 26-04-0024 and in part by B-K Medical Aps, Herlev, Denmark. *Asterisk indicates corresponding author.*

*J. A. Jensen is with the Center for Fast Ultrasound Imaging, Technical University of Denmark, DK-2800 Lyngby, Denmark.

N. Oddershede with the Center for Fast Ultrasound Imaging, Technical University of Denmark, DK-2800 Lyngby, Denmark.

Digital Object Identifier 10.1109/TMI.2006.883087

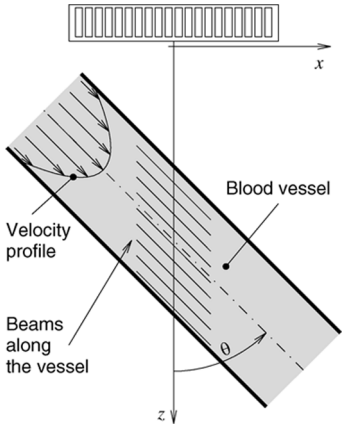

Fig. 1. Beamforming is made along the laminar flow. Figure from [8].

can be correlated to obtain the velocity of the blood or tissue [14]. It is here important that the two images are acquired in a short time interval, and that the emission sequence is exactly the same to maximize correlation. The recursive image formation can also be employed here and a new correlation function estimate formed after each emission. It is vital that the image formation sequence is exactly the same and high-resolution images N_t emissions apart should only be correlated. The correlation functions can, however, be averaged for all emissions, if the velocity is constant [14].

SA flow imaging has several advantages compared to traditional ultrasound flow imaging. The primary one is the continuously available data for all points in the image. The velocity estimation can, therefore, take place continuously, the initialization of stationary echo canceling filters becomes trivial, and the number of samples for velocity estimation are only restricted by the time for which the flow can be assumed quasi-stationary.

Another advantage of SA flow imaging is that data can be focused in any direction. It is, thus, possible to focus signals along the flow direction as suggested in [7] and shown in Fig. 1. Here, a three-dimensional (3-D) cartesian coordinate system with origo at the center of the transducer surface is used, where x follows the lateral direction, y the elevation direction, and z the axial direction. The high-resolution image data are then beamformed along the direction of the flow. The focusing points are given by $\vec{r}_p(k) = [\Delta r \cdot k \cdot \sin(\theta), 0, \Delta r \cdot k \cdot \cos(\theta) + z_{st}]$, where Δr is spatial sampling interval, k sample index, θ flow angle between the flow vector and z-axis, and z_{st} depth of the vessel. The data are focused for each emission and the final high-resolution directional signal is obtained by adding all N_t low-resolution images L_j

$$y_d^{(n)}(k) = \sum_{j=n-N_t+1}^{n} L_j(\vec{r}_p(k)). \tag{1}$$

The spatial movement between high-resolution images is $\vec{d}_s = \vec{v} T_{\mathrm{prf}} N_t$, where the blood velocity is $\vec{v} = |\vec{v}|[\sin\theta, 0, \cos\theta]$, and T_{prf} is the pulse repetition period. This distance corresponds to a sample index of

$$k_s = \frac{|\vec{v}| T_{prf} N_t}{\Delta r}. \tag{2}$$

Correlating two received signals over $N_k + 1$ samples from two high-resolution images gives

$$\begin{aligned} R_{12}(l) &= \frac{1}{N_k+1} \sum_{k=-N_k/2}^{N_k/2} y_d^{(n)}(k) y_d^{(n+N_t)}(k+l) \\ &= \frac{1}{N_k+1} \sum_{k=-N_k/2}^{N_k/2} y_d^{(n)}(k) y_d^{(n)}(k+l-k_s) \\ &= R_{11}(l-k_s) \end{aligned} \tag{3}$$

where $y_d^{(n)}(k)$ is the directional signal focused after emission n and $R_{11}(l)$ is its autocorrelation function.

A global maximum is found at $l = k_s$ and the velocity magnitude is estimated from

$$|\vec{v}| = \frac{k_s \Delta r}{T_{\mathrm{prf}} N_t}. \tag{4}$$

The spatial sampling interval Δr must be below $\lambda/4$ to obey the sampling criterion, where λ is the wavelength, but reducing Δr increases the amount of beamformation. Parabolic interpolation [15], [16] is used to increase the precision of the estimated velocity.

III. Determination of Velocity Angle

The velocity angle for beam formation has previously been determined manually from the B-mode image, and this section introduces an automatic approach for determining the angle.

The primary reason for decorrelation of traditional flow signals is the velocity distribution within the range gate. This makes part of the scatterers travel faster or slower than others, which decorrelates the received signal from emission to emission. Directional beamforming along the true flow direction avoids the decorrelation, since it tracks the scatterers in the correct direction and thereby maintains a high correlation. When beamforming along all other directions, the signals will again decorrelate. This observation is used to devise a method for automatic angle determination. The correlation peak found for the correct angle normalized by the power of the signal must, therefore, have the highest correlation values, since it has the least decorrelation due to a velocity distribution. This is stated as

$$R_{12n}(\theta_m) = \left(\frac{\max(R_{12}(l, \theta_m))}{R_{11}(0, \theta_m)} \right) \tag{5}$$

$$\theta = \underset{\theta_m}{\mathrm{Arg\ min}}\, R_{12n}(\theta_m) \tag{6}$$

where $\max(R_{12}(l, \theta_m))$ is the maximum value of the cross-correlation function for the angles θ_m and $R_{11}(0, \theta_m)$ is the corresponding power of the signal. The correct angle θ is found where the normalized correlation function as a function of angle $R_{12n}(\theta_m)$ has its peak value.

An example of the calculated normalized correlation is shown in Fig. 2 for a true angle of 90°. The data are from the measurements described in Section V. The correlation has been calculated for every 2°, and the global maximum coincides with the correct angle.

The resolution in angle determination is here equal to 2°, which is less accurate than desired. An interpolated value using

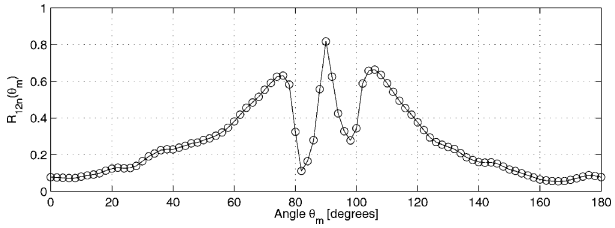

Fig. 2. Normalized maximum correlation as a function of beam formation angle. Circle show the values for the individual estimates.

a parabolic approximation of the peak is calculated for the angle as [15], [16]

$$\theta_{\text{int}} = \theta - \frac{R_{12n}(\theta+\Delta\theta) - R_{12n}(\theta-\Delta\theta)}{2(R_{12n}(\theta+\Delta\theta) - 2R_{12n}(\theta) + R_{12n}(\theta-\Delta\theta))}\Delta\theta \tag{7}$$

to avoid having to calculate the directional signals for too many directions. Here, $\Delta\theta$ is the angle sampling interval. The number of values can of course be narrowed down, if prior information can be used to determine a rough estimate. This could be from either temporal or spatial neighbors to the current estimate.

IV. Simulation

The angle determination method was tested along a wide range of flow angles using simulated data from the simulation program Field II [17], [18]. A parabolic flow was simulated inside a 10-mm-long cylinder with a radius of 2.5 mm, centered at $[x, y, z] = [0, 0, 37.5]$ mm. The cylinder was rotated to the angle θ, as shown in Fig. 1. For each volume of λ^3, where λ is the wavelength given in Table I, 10 scatterers were randomly distributed, and their amplitudes were generated from a Gaussian distribution with zero mean. At each emission, the scatterers were propagated according to their radial position

$$d_\theta = v_0 T_{prf}\left(1 - \left(\frac{r}{R}\right)^2\right), \quad r < R \tag{8}$$

where d_θ is the distance propagated along θ at each emission, v_0 is the peak velocity, r is the radial position of the scatterer, and R is the cylinder radius. As the scatterers reached the cylinder end, they were feed back to the beginning.

A 7-MHz commercial linear array transducer was simulated. The simulations have been performed by using eight emissions equally spread over the 128 element aperture, with each emission using 11 defocused elements to emulate a spherical wave emission [10]. A frequency encoded chirp is used in transmission, which in measurement situations will increase the signal-to-noise ratio (SNR) [19], [12]. The chirp has a duration of 20 μs and a bandwidth of 7 MHz centered around the transducer center frequency. Only 64 receiving elements are used at each reception, and they are multiplexed to be closest to the emitting center element, and all 128 receiving elements are hereby sampled. The transmission is repeated with a pulse repetition frequency of 3 kHz and 1280 individual emissions have been simulated by repeating the sequence 160 times. A summary of the parameters used for simulation and processing is shown in Table I.

The received radio frequency (RF) element signals are first matched filtered to compress the signals in the axial direction and increase the SNR [19]. The resulting signals are beamformed along every 5° covering a total of 180°. Hereby, low-resolution directional signals are formed, and high-resolution signals are made by adding the latest eight low-resolution signals. Stationary echo canceling is performed separately for each direction by finding the mean value of the focused lines and then subtracting this from the signals. The focused directional signals from the same image formation are subsequently cross-correlated and added to the other cross-correlation functions, and the velocity angle is found from the combined cross-correlation function, as described in Section III.

Ten simulations at flow angles θ equally spaced from 0° (axial flow) to 90° (lateral flow) have been performed. The velocity angle was found in the center of the cylinder from 16 sequences of eight emissions, each corresponding to a total of 128 emissions. Hereby, 10 independent estimates are made from the 1280 emissions. The bias and standard deviation of the angle estimates have been calculated and is plotted in Fig. 3 as a function of the true flow angle.

Both the bias and standard deviation of the angle estimates are below 3° for flow angles from $\theta = 20°$ to 90°. At flow angles of 0° (axial flow) and 10°, an unfortunate combination of the flow velocity and the pulse repetition frequency result in higher bias and standard deviation. Here, the propagation between shots at the vessel center coincide with a quarter of a wavelength $d_\theta \approx \lambda/4$, resulting in a reduction of the SNR and an increase in sidelobes levels [20]. A higher pulse repetition frequency than 3 kHz would solve this problem [20].

TABLE I
Parameters for Transducer and Parabolic Flow Simulation

Center frequency	f_0	7 MHz
Wavelength	$\lambda = c/f_0$	0.22 mm
Element pitch	w	0.208 mm
Element height	h_e	4.5 mm
Number of receive elements	N_r	128
Number of transmit events	N_t	8
Elevation focus	R_e	20 mm
Directional signals	N_e	128
Pulse repetition frequency	f_{prf}	3 kHz
RF sampling frequency	f_s	120 MHz
Distance between estimates	dz	0.25 mm
Sampling interval for lines	$\Delta r = \lambda/20$	0.011 mm
Correlation interval	$-10\lambda : 10\lambda$	-2.2:2.2 mm
Radius of vessel	R	2.5 mm
Distance to vessel center	z_{st}	37.5 mm
Peak velocity in flow	v_0	0.15 m/s
Simulated flow angles	θ	$0°, 10°, .., 90°$

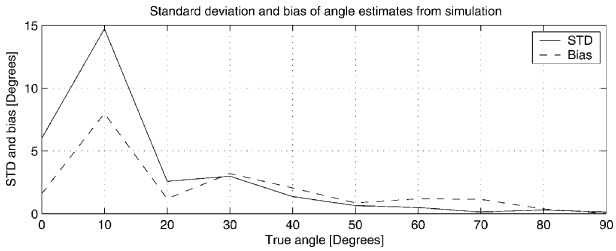

Fig. 3. Standard deviation and bias for 10 independent velocity angle estimates in the center of the simulated blood vessel. Simulation is repeated for angles $\theta = 0°, 10°, \ldots, 90°$. Dashed line shows the bias, and the solid line shows the standard deviation as a function of the true angle θ.

TABLE II
STANDARD PARAMETERS FOR TRANSDUCER AND PARABOLIC FLOW MEASUREMENT

Center frequency	f_0	7 MHz
Wavelength	$\lambda = c/f_0$	0.22 mm
Element pitch	w	0.208 mm
Element height	h_e	4.5 mm
Number of receive elements	N_r	128
Number of transmit events	N_t	8
Elevation focus	R_e	20 mm
Directional signals	N_e	128
Pulse repetition frequency	f_{prf}	3 kHz
RF sampling frequency	f_s	40 MHz
Distance between estimates	dz	0.25 mm
Sampling interval for lines	$\Delta r = \lambda/20$	0.011 mm
Correlation interval	$-10\lambda : 10\lambda$	-2.2:2.2 mm
Radius of vessel	R	8.5 mm
Distance to vessel center	z_{st}	37.5 mm
Peak velocity in flow	v_0	0.15 m/s

V. MEASUREMENTS

The angle determination method was also investigated using a circulating flow rig. A Smedegaard EcoWatt 1 pump circulates a blood mimicking fluid made by Danish Phantom Service consisting of water, glycerol, orgasol, Trition x-100, NaBenzoat, and K_2EDTA diluted 10 to 1 with demineralised water. A reduction valve was used to control the velocity. The tubing consisted of a 1.2-m-long, 20-mm-diameter steel tube before the flow entered a 18-mm-diameter heat shrink tubing. The thickness of the heat shrink tubing was 0.5 mm giving an internal diameter of 17 mm. The flow was maintained with a peak velocity less than 0.15 m/s giving a Reynolds number of 1276 assuming a viscosity of 2 cP and a parabolic profile.

Measurements were performed using the RASMUS research scanner [21]. It can emit arbitrary signals in 128 individual channels and can simultaneously sample signals from 64 receive channels at 40 MHz with 12-bits precision. A two-to-one multiplexing makes it possible to cover all 128 transducer elements in twp emissions. Data are stored in the system's 16 GB of memory in real-time, and they are transferred to a Linux computer cluster with 100 CPUs for beam formation and velocity estimation.

The 7-MHz commercial linear array transducer previously simulated was also used in the experiments. It was mounted in a fixation device above the tube at a certain beam to flow angle and at a certain distance from the tube center. The transmission sequence was the same as for the simulations, again using a linear chirp and generating spherical waves from eight different locations each time using 11 defocused elements. A total of 3000 individual emissions was acquired by repeating the sequence 375 times. A summary of the parameters used for data acquisition and processing is shown in Table II. The data is the same as that used in [8] for investigating the velocity estimation.

Two experiments at flow angles θ of 60° and 90° (transverse velocity) were performed. The velocity along the flow direction was found from 16 sequences of eight emissions, each corresponding to a total of 128 emissions. This is the same number of emissions that is used in normal spectral velocity imaging [2] over which the flow normally can be considered quasi-stationary in the human body. The velocity could be estimated with a standard deviation over the whole profile of 0.36% relative to the peak velocity of the vessel for a velocity angle of 60°. The standard deviation was 1.2% for 90° [7].

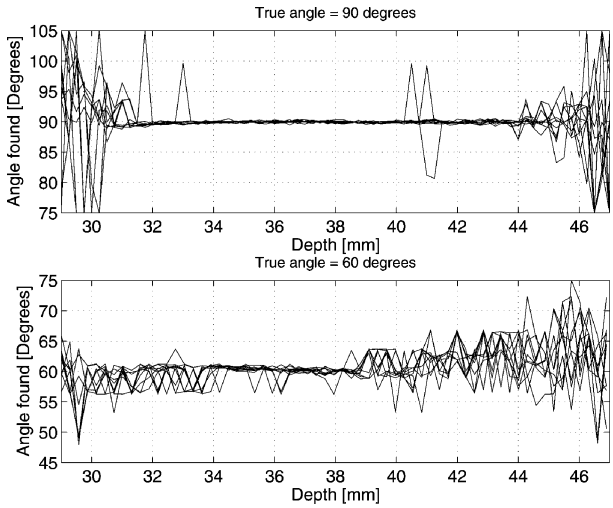

Fig. 4. Estimated velocity angles for a true velocity angle of 90° (top) and 60° (bottom).

The angle determination method has been applied on the data and the results are shown in the bottom part of Fig. 4 for a true velocity angle of 60°. One line is shown for each of the 10 independent velocity estimates, and the velocity has been found for 180° in steps of 5°. The vessel boundaries are between 30 and 46 mm. Here, the mean value of all estimates is 60.54° and the standard deviation is 2.1°. A slight increase in standard deviation as a function of depth is seen. This is probably due to the decrease in SNR as a function of depth.

The same experiment has been repeated for a true velocity angle of 90° and the result is shown in the top part of Fig. 4. Here, the mean value is 90.0003° and the standard deviation is 1.32°. The standard deviation rises sharply at the edges of the vessel. Here, the velocity is low and the echo canceling will remove most of the signal power. The SNR is, thus, low and the accuracy of the estimates is thereby low. The standard deviation and bias are, therefore, found using only data inside the vessel to avoid domination by these edge effects.

The velocity magnitude profiles after both angle and velocity estimation can be seen in Fig. 5. First, the angle has been determined and then the corresponding velocity for the angle has been used as the velocity magnitude. No interpolation between the 5° angle estimates have been performed, before the velocity magnitude was determined, and the velocity is just found at the angle with the peak normalized correlation given by (6). The top graph shows the ten profiles at 90° and the bottom at 60°. The standard deviation of data averaged over the profile at 60° is 0.0046 m/s or 2.9% relative to the peak velocity. At 90°it is 0.0034 m/s or 2.1397%. The standard deviation is, thus, somewhat increase compared to when no determination of angle is used.

VI. PARAMETER STUDY

A parameter study has been performed on the data described in the previous section. Here, the influence of a variation in the number of lines and the correlation length has been performed

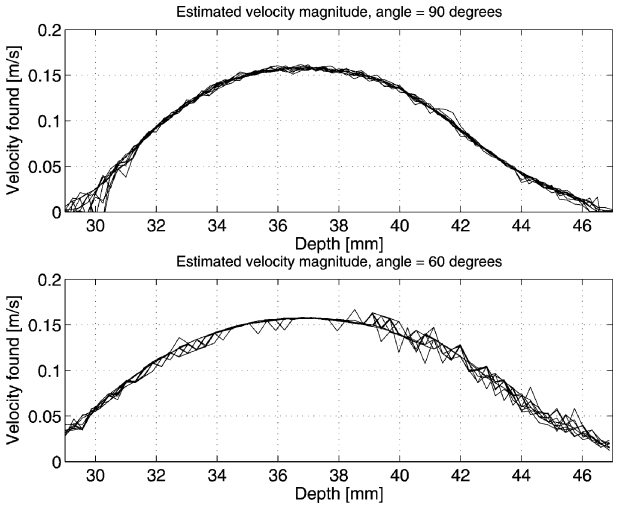

Fig. 5. Estimated velocity magnitude for a true velocity angle of 90° (top) and 60° (bottom).

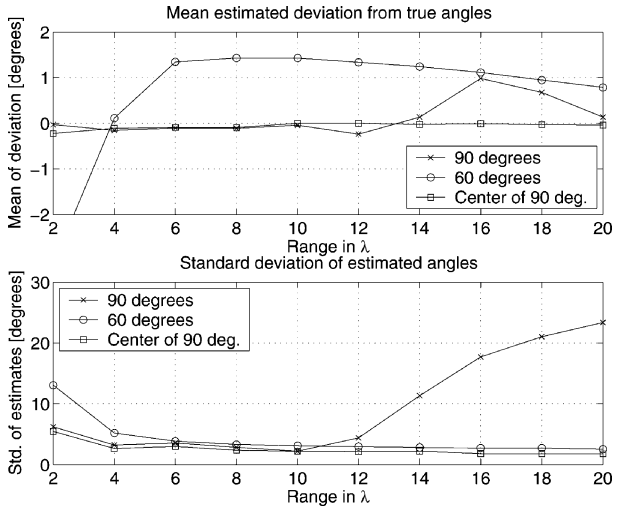

Fig. 6. Variation in correlation range in terms of the wavelength λ. Upper graph shows the bias of the angle estimates and the lower graph shows the standard deviation. Circled line is for the 60° experiment, the crossed line is for the 90° experiment, and the squared line is for the center part of the tube at 90°.

for the 60° and 90° data sets. The standard parameters shown in Table II are used for the processing.

In Fig. 6, the variation in the mean estimated deviation from the true angle is shown in the top graph as a function of correlation interval given as a multiple of the wavelength λ. The correlation is over an interval of $\pm$ the range given on the figures x axis. A value of 10, thus, indicates a correlation range of $-10\lambda : 10\lambda$. The bias and standard deviation have been found in the center of the vessel, which is from 31.8 to 44.1 mm at 90° and from 31.8 to 46.0 mm at 60°. Hereby the angle is only found in the center part of the vessel and the uncertain and less important estimates at the edges are excluded. The standard deviation is shown in the lower graph in Fig. 6. For all ranges above 4λ, the bias is below 2° at 60° and below 1° at 90° flow angles. The std. also drops for increasing range, since more data is available in the correlation for 60°. At 90°, the standard decreases until 10λ after which it increases. The standard drops in the middle

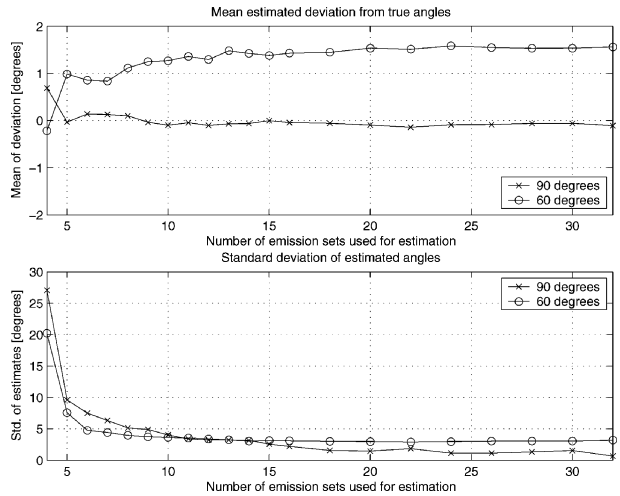

Fig. 7. Variation in number of lines used in the cross-correlation function. One set consists of eight emissions for creating a high-resolution image or line. Circles mark the 60° experiment, and the crosses mark the 90° experiment.

of the vessel but rises at the edges, since the correlation range is so large, that directional lines reaches outside the vessel and this affects the angle estimator. The graph with the squares show the performance in the central core of the vessel at depths between 33.7 and 43 mm. Here, there are no edge effects and the standard deviation and bias decreases with increasing correlation range. It is, thus, not advisable to have too long directional lines in this case, and lower ranges are also an advantage, when nonlaminar flow patterns and turbulence are encountered.

Fig. 7 shows the performance as a function of number of high-resolution images employed in the estimation process. Each sets corresponds to eight emissions that makes up a high-resolution image. For this stationary flow measurement, it is an advantage to use more lines as both mean deviation (top) and standard deviation (bottom) is reduced for an increasing number of sets. For 60°, the bias does no decrease and this might be due to a misalignment of the vessel, so that the true angle is closer to 61.5° than 60°.

VII. Vector Velocity Image

The acquired data can be used to find both direction and velocity magnitude for a full image from the 128 emissions. Such a velocity vector image is shown in Fig. 8. The velocity vector is found for every 1 mm in the lateral and axial direction, and the velocity magnitude and direction are shown as arrows with a length proportional to velocity. The underlying velocity color map has been made from the estimates by interpolating the values by a factor of 10 in each direction and encode the color from the velocity magnitude. Only velocity estimates above a magnitude of 0.005 m/s are shown and else the underlying B-mode image is shown. The B-mode image has been made from eight emissions and a dynamic range of 40 dB is used. Most of the vessel is filled with color and the direction is found to be 90° at nearly all locations.

A similar image for 60° is shown in Fig. 9. The lower left corner shows erroneous velocity estimates, which is due to lack of signal. Only noise is present in this part and random velocity vectors are, thus, found. These could be removed by employing

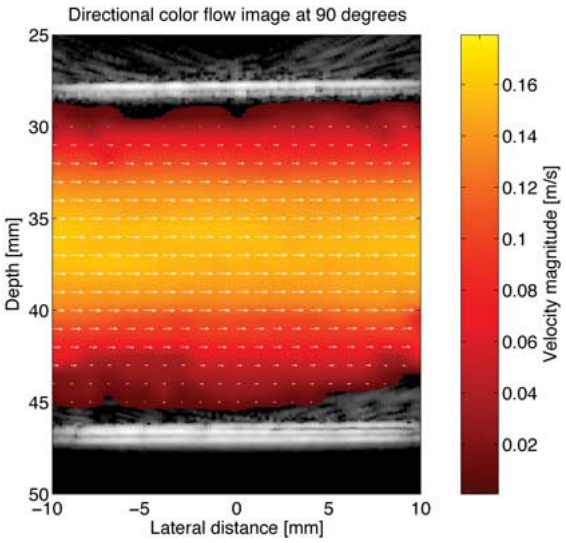

Fig. 8. Vector velocity image for a true velocity angle of 90°. Both magnitude and directions are estimated.

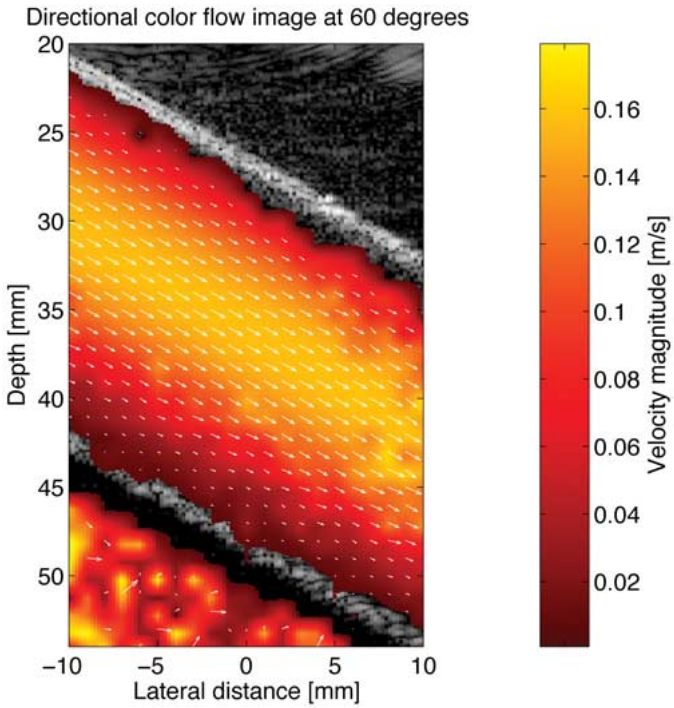

Fig. 9. Vector velocity image for a true velocity angle of 60°. Both magnitude and directions are estimated.

a discriminator using the energy of the signals and excluding estimates only based on noise. The energy is found as

$$E = \sum_{n=1}^{N_l} \sum_{k=-N_k/2}^{N_k/2} (y_d^{(n)}(k))^2 \tag{9}$$

where $N_k + 1$ is the number of samples in the directional lines and N_l is the number of directional signal used for a single velocity estimation. This could be compared to the expected noise energy of current setup.

TABLE III
PARAMETERS USED FOR THE EXPERIMENT

Transducer type	Linear array
Number of transducer elements	128
Transducer element pitch	0.3 mm
Transducer element kerf	0.035 mm
Transducer element height	5 mm
Elevation focus	20 mm
Center frequency, f_0	6.2 MHz
Wavelength, $\lambda = c/f_0$	0.25 mm
Excitation type	20 μs tapered chirp
Frequencies swept	$\sim$ 3 - 8 MHz
Number of emitting elements	11
Number of receiving elements	64, centered at em.
Number of emissions in sequence, N_t	8
Number of virtual sources, $(= N_t)$	8
Virtual source positions	[x, 0, -2.5] mm
Pulse repetition frequency, f_{prf}	10 kHz
Points in line, $N_k + 1$	401
Spatial sampling interval, Δr	$\lambda/20 = 12.5\mu$m
Line length	$20\lambda = 5$ mm
Angular sampling interval, $\Delta\theta$	5°
Stationary echo canceling method	Linear regression [23]
Number of correlations averaged, L	113
Velocity search range	-1.5 to 1.5 m/s

VIII. *In Vivo* MEASUREMENTS

This section shows examples for *in vivo* data. 2.2 s of real-time *in vivo* data of the common carotid artery of a healthy 30-year-old male volunteer was acquired using the RASMUS multichannel sampling system [21] and a 128 element linear array transducer. The scanning was done by an experienced sonographer. Data processing was performed offline on a 100 CPU computer cluster. The parameters used for data acquisition and processing are outlined in Table III.

Due to hardware limitations, only 64 elements of the full 128 element array was used at reception. The receiving subaperture was slid at each emission to be centered around the emitting subaperture. The excitation waveform was a 20-μs chirp linearly sweeping frequencies from 3 to 8 MHz, amplitude tapered by a 10% Tukey window. The received signals were compressed using a mismatch compression filter, which was the time-inverse chirp tapered by a Chebyshev window with 70% relative sidelobe attenuation [22].

Data were processed in blocks of 128 emissions corresponding to 12.8 ms of data. The flow angle was estimated for every data block, as described in Section III for a 1-mm grid of points ranging from 16 to 31 mm depth and -10 to 10 mm lateral. The velocity magnitude was estimated along the angle found for each individual point. The estimation process for each point was therefore mutually independent.

B-mode images were simply made by beamforming high-resolution lines along the axial direction followed by envelope detection and logarithmic compression. All B-mode images are shown in 30-dB dynamic range only. The reason for the low B-mode image quality compared to that of [24] is found in the sparse emission sequence used for flow estimation. A solution could be to make interleaved emission sequences of both B-mode and flow emissions.

Full 2-D vector flow images were made by combining B-mode images with both colors indicating velocity magnitude

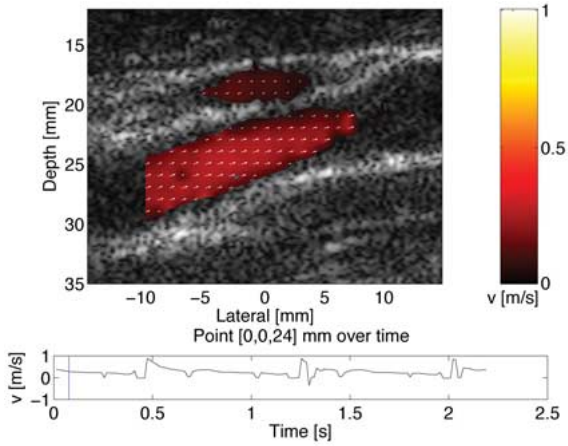

Fig. 10. Synthetic aperture vector flow image of the common carotid artery and jugular vein at middiastole. Vertical line in the bottom part marks the time of the image.

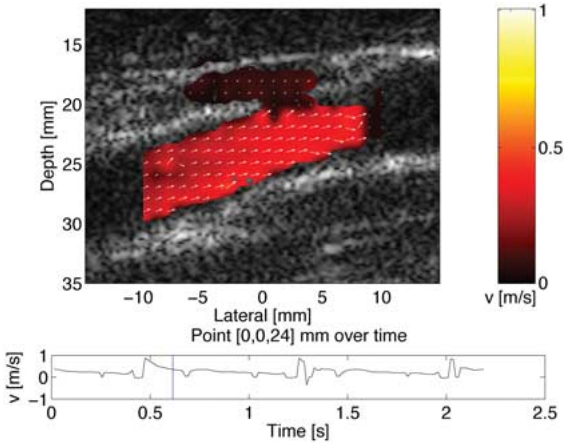

Fig. 11. Synthetic aperture vector flow image of the common carotid artery and jugular vein at end systole. Vertical line in the bottom part marks the time of the image.

and vector arrows showing the estimated flow direction and velocity magnitude. Velocity estimates were displayed when the energy of the directional signals after stationary echo canceling was above a certain fraction of the energy of the signals prior to echo canceling. This can be written as

$$\frac{\sum_{n=1}^{N_l}\sum_{k=-N_k/2}^{N_k/2}\mathrm{SEC}[(y_d^{(n)}(k))^2]}{\sum_{n=1}^{N_l}\sum_{k=-N_k/2}^{N_k/2}(y_d^{(n)}(k))^2} > E_f \tag{10}$$

where $\mathrm{SEC}[\cdot]$ denotes the stationary echo canceling operation, N_k+1 is the number of samples in the directional lines, N_l is the number of directional signal used for a single velocity estimation, and E_f is the required energy fraction.

Fig. 10 shows a synthetic aperture vector flow image made at mid-diastole. Both the common carotid artery and a cross section of the jugular vein is seen. The base of each vector arrow shows the point of estimation, and the vector direction and length indicates the flow angle and magnitude, respectively. The bottom plot indicates the velocity at point [0,0,24] mm over the entire 2.2 s of data, and the vertical bar indicates the time of the current frame. The peak systoles occur around time $t = 0.5, 1.3,$ and 2.0 s.

A vector flow image made at end systole is shown in Fig. 11. The increased velocity is indicated both by a lighter color, and by the increased length of the vector arrows. A slight discrimination problem between tissue and blood is seen at the border between the carotid artery and the jugular vein.

Fig. 12 shows a vector flow image made at peak systole. Dark velocity vectors are used for better visualization. In the vessel center, the majority of the angle estimates are within the expected range, but close to the vessel border the performance is poor. This is mainly due to problems of suppressing the large vessel border movements during the systolic phase.

The top plot of Fig. 13 shows the estimated angles for a point in the center of the common carotid artery over time. The majority of the estimates are centered around $\theta = 106°$ which corresponds to the flow angle visually determined from the B-mode

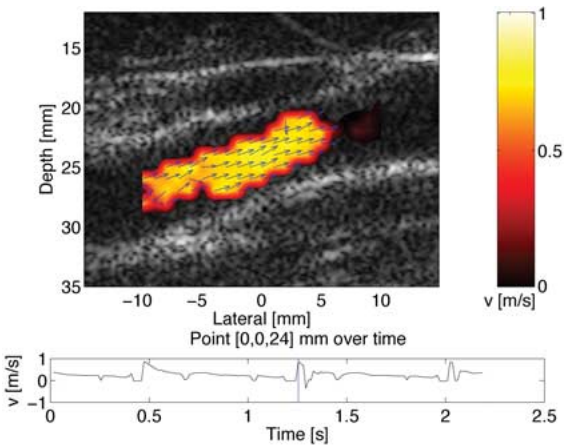

Fig. 12. Synthetic aperture vector flow image of the common carotid artery and jugular vein at peak systole. Vertical line in the bottom part marks the time of the image.

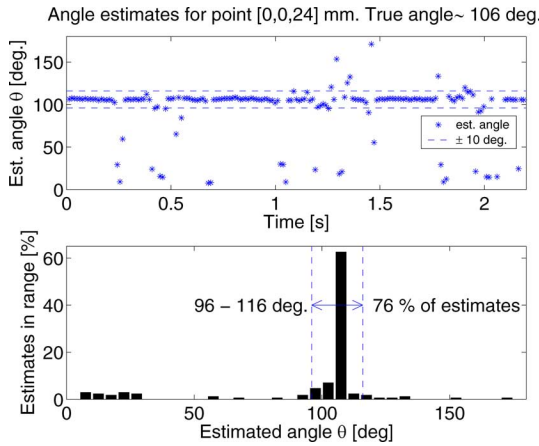

Fig. 13. Top plot show the individual angle estimates for a point in the center of the common carotid artery [0,0,24] mm over time. Bottom plot shows a histogram of the flow angle estimates, indicating that 76% of the estimates are within $\pm 10°$ of the flow angle of $106°$ visually determined from the B-mode image.

image (see Fig. 10). The bottom plot shows a histogram of the angle estimates, where 76% of the 171 estimates are within the

range of $106° \pm 10°$, which is considered adequate for finding the velocity magnitude. These estimates within the $\pm 10°$ range have a standard deviation below $2.7°$. 69% of the estimates are within the range of $106° \pm 5°$. There seems to be a tendency for an increasing number of false estimates around time $t = 0.5$, 1.3, and 2.0 s where the peak systoles are found. Furthermore, it is noticed that the majority of the erroneous estimates are close to perpendicular to the flow direction, indicating that the suppression of the high amplitude tissue signal by the stationary echo canceling filter is not optimal. This can potentially be solved by applying more advanced stationary echo canceling filters.

IX. Conclusion

An approach for determining both velocity magnitude and angle in a SA flow system has been presented. For data measured using an experimental ultrasound scanner and a flow rig, both magnitude and angle could be determined with a relative standard deviation of roughly 2% for flow angles of 60° and 90°. A parameter study showed the influence of the number of lines in an estimate and the correlation length.

The synthetic aperture 2-D vector velocity estimation method was applied to *in vivo* data from the human common carotid artery. Full color flow maps including 2-D vectors showing the flow direction were presented from both the diastolic and systolic phase. For a point in the vessel center, the flow angle is estimated over time and 76% of the estimates were within $\pm 10°$ of the flow direction visually determined from the B-mode image.

Acknowledgment

The authors would like to thank M. B. Nielsen and K. R. Nielsen, both from the Department of Radiology, Section of Ultrasound, Rigshospitalet, Denmark, for performing the clinical scanning, and S. Nikolov for making the measurements in the flow rig.

References

[1] D. H. Evans, W. N. McDicken, R. Skidmore, and J. P. Woodcock, *Doppler Ultrasound, Physics, Instrumentation, and Clinical Applications*. New York: Wiley, 1989.

[2] J. A. Jensen, *Estimation of Blood Velocities using Ultrasound: A Signal Processing Approach*. New York: Cambridge Univ. Press, 1996.

[3] G. E. Trahey, J. W. Allison, and O. T. von Ramm, "Angle independent ultrasonic detection of blood flow," *IEEE Trans. Biomed. Eng.*, vol. BME-34, pp. 965–967, 1987.

[4] M. D. Fox, "Multiple crossed-beam ultrasound Doppler velocimetry," *IEEE Trans. Son. Ultrason.*, vol. SU-25, pp. 281–286, 1978.

[5] O. Bonnefous, "Statistical analysis and time processes applied to velocity measurement," in *Proc. IEEE Ultrason. Symp.*, 1989, pp. 887–892.

[6] J. A. Jensen and I. R. Lacasa, "Estimation of blood velocity vectors using transverse ultrasound beam focusing and cross-correlation," in *Proc. IEEE Ultrason. Symp.*, 1999, vol. 2, pp. 1493–1497.

[7] J. A. Jensen and S. I. Nikolov, "Transverse flow imaging using synthetic aperture directional beamforming," *Proc. IEEE Ultrason. Symp.*, vol. 2002, no. 2, pp. 1488–1492, 2002.

[8] ——, "Directional synthetic aperture flow imaging," in *IEEE Trans. Ultrason. Ferroelec. Freq. Contr.*, Sep. 2004, vol. 51, no. 9, pp. 1107–1118.

[9] J. A. Jensen, "Velocity vector estimation in synthetic aperture flow and B-mode imaging," in *IEEE Int. Symp. Biomed. Imag. Nano Macro*, Apr. 2004, vol. 1, pp. 32–35.

[10] M. Karaman, P. C. Li, and M. O'Donnell, "Synthetic aperture imaging for small scale systems," *IEEE Trans. Ultrason. Ferroelectr. Freq. Control*, vol. 42, no. 3, pp. 429–442, May 1995.

[11] G. R. Lockwood, J. R. Talman, and S. S. Brunke, "Real-time 3-D ultrasound imaging using sparse synthetic aperture beamforming," *IEEE Trans. Ultrason. Ferroelectr. Freq. Control*, vol. 45, no. 4, pp. 980–988, Jul. 1998.

[12] K. L. Gammelmark and J. A. Jensen, "Multielement synthetic transmit aperture imaging using temporal encoding," *IEEE Trans. Med. Imag.*, vol. 22, no. 4, pp. 552–563, Apr. 2003.

[13] S. I. Nikolov, K. Gammelmark, and J. A. Jensen, "Recursive ultrasound imaging," in *Proc. IEEE Ultrason. Symp.*, 1999, vol. 2, pp. 1621–1625.

[14] S. I. Nikolov and J. A. Jensen, "In-vivo synthetic aperture flow imaging in medical ultrasound," *IEEE Trans. Ultrason. Ferroelectr. Freq. Control*, vol. 50, no. 7, pp. 848–856, Jul. 2003.

[15] S. G. Foster, "A pulsed ultrasonic flowmeter employing time domain methods," Ph.D. dissertation, Dept. Elec. Eng., Univ. Illinois, Urbana, Il, 1985.

[16] S. G. Foster, P. M. Embree, and W. D. O'Brien, "Flow velocity profile via time-domain correlation: Error analysis and computer simulation," *IEEE Trans. Ultrason. Ferroelectr. Freq. Control*, vol. 37, no. 3, pp. 164–175, May 1990.

[17] J. A. Jensen, "Field: A program for simulating ultrasound systems," in *Med. Biol. Eng. Comp.*, 1996b, vol. 4, 10th Nordic-Baltic Conference on Biomedical Imaging, pp. 351–353.

[18] J. A. Jensen and N. B. Svendsen, "Calculation of pressure fields from arbitrarily shaped, apodized, and excited ultrasound transducers," *IEEE Trans. Ultrason. Ferroelectr, Freq. Control*, vol. 39, no. 2, pp. 262–267, Mar. 1992.

[19] T. X. Misaridis and J. A. Jensen, "An effective coded excitation scheme based on a predistorted FM signal and an optimized digital filter," in *Proc. IEEE Ultrason. Symp.*, Oct. 1999, vol. 2, pp. 1589–1593.

[20] N. Oddershede and J. A. Jensen, "Effects influencing focusing in synthetic aperture vector flow imaging," *IEEE Trans. Ultrason. Ferroelectr. Freq. Control*, 2006, submitted for publication.

[21] J. A. Jensen, O. Holm, L. J. Jensen, H. Bendsen, S. I. Nikolov, B. G. Tomov, P. Munk, M. Hansen, K. Salomonsen, J. Hansen, K. Gormsen, H. M. Pedersen, and K. L. Gammelmark, "Ultrasound research scanner for real-time synthetic aperture image acquisition," *IEEE Trans. Ultrason. Ferroelec. Freq. Control*, vol. 52, no. 5, pp. 881–891, May 2005.

[22] T. Misaridis, Ultrasound imaging using coded signals. Lyngby, Denmark, Technical University of Denmark (DTU), 2001, Ph.D. dissertation.

[23] A. P. G. Hoeks, J. J. W. van de Vorst, A. Dabekaussen, P. J. Brands, and R. S. Reneman, "An efficient algorithm to remove low frequency Doppler signal in digital Doppler systems," *Ultrason. Imag.*, vol. 13, pp. 135–145, 1991a.

[24] M. H. Pedersen, K. L. Gammelmark, and J. A. Jensen, "Preliminary in-vivo evaluation of convex array synthetic aperture imaging," *Proc. SPIE – Progress in Biomedical Optics and Imaging*, pp. 33–43, 2004.